Progress In Electromagnetics Research, Vol. 126, 355–373, 2012

A NOVEL DIELECTRIC CONFORMAL FDTD METHOD FOR COMPUTING SAR DISTRIBUTION OF THE HUMAN BODY IN A METALLIC CABIN ILLUMINATED BY AN INTENTIONAL ELECTROMAGNETIC PULSE (IEMP)

L.-Y. Kong[1], J. Wang[1, *], and W.-Y. Yin[1, 2]

[1]Center for Microwave and RF Technologies, Key Lab of Ministry of Education for Design and EMC of High-Speed Electronic Systems, Shanghai Jiao Tong University, Shanghai 200240, China

[2]Center for Optical and EM Research (COER), State Key Lab of MOI, Zhejiang University, Hangzhou 310058, China

Abstract—One novel dielectric conformal finite-difference time-domain (FDTD) method is used for computing specific absorption rate (SAR) distribution over the human body model in one metallic cabin with some windows on its wall. It is based on the concept of area average, which is different from other traditional conformal FDTD schemes. Our developed algorithm is verified by calculating both point and average SARs of dielectric sphere and human head models illuminated by an intentional electromagnetic pulse (IEMP), respectively, and CST Microwave Studio (MWS) also used for validating its accuracy. Numerical calculations are further performed to show the average SAR distribution over the human body model for different IEMP incidences, where the cabin door is opened or closed. The effects of E-field amplitude, direction and polarization of the incident IEMP on the SAR distributions are characterized in detail. This study will be useful for further electromagnetic protection for some persons working in high power exposure environment.

Received 27 November 2011, Accepted 5 March 2012, Scheduled 22 March 2012

* Corresponding author: Jian Wang (wangjianmath@sjtu.edu.cn).

1. INTRODUCTION

Metallic cabins or enclosures have been widely used for protecting various electronic circuits and communication systems from the attack of certain intentional electromagnetic pulse (IEMP), which can be generated by high-power antennas, nuclear explosions and highly directed electromagnetic weapons [1], etc. In their practical applications, one door and some windows have to be introduced on the cabin wall, which provide directive coupling paths for an IEMP, resulting in serious degradation in their protecting or shielding effectiveness. Therefore, in the past two decades, some theoretical and experimental studies have been carried out for the design of metallic rectangular cabins with high protecting effectiveness, together with their inner field prediction using the method of moments (MoM) as well as finite-difference time-domain (FDTD) method [2–4].

On the other hand, we know that some very effective three-dimensional (3-D) FDTD algorithms have been reported recently for predicting biological effects due to electromagnetic exposure, in particular for SAR computation of the human head or body in the presence of a non-intentional electromagnetic radiation [5–17]. However, it must be understood that, in order to obtain an accurate SAR solution for the human head or body using the FDTD method, the spatial mesh size should be small enough so as to effectively suppress its staircase errors. Under such circumstances, both sub-gridding and conformal FDTD methods can be used for improving their simulation efficiencies [18–24]. On the other hand, we have to say that the former is difficult for eliminating reflection from the boundaries between coarse and fine cells, and it often introduces an unexpected unstable problem. The conformal FDTD method, adopting the Yee's cells and keeping the original computational domain and time steps, can be employed to handle one three-dimensional object with an arbitrary geometry. However, in the presence of an IEMP with high power, using the conformal FDTD method to compute the SAR distribution of the human body inside one metallic cabin with large sizes has not been reported yet, which is very important for carrying out an effective electromagnetic protection for people working in one complex electromagnetic environment. That is the main motivation behind this study.

In this paper, one modified dielectric conformal FDTD method is used for computing SAR distribution of a human body in a large metallic cabin, in which magnetic grid is adopted and effectively constitutive parameters of the conformal cells are obtained by the weighted-area of dielectric and free space. The predicted SAR

distributions of both dielectric sphere and human head models obtained by our method agree well with those of CST Microwave Studio (MWS). We further apply this conformal FDTD method to compute SAR distributions of the human body model in one metallic cabin with large sizes illuminated by an external IEMP for different power levels, incident directions and polarizations.

2. PROBLEM DESCRIPTION

Figure 1 shows the geometry of a large metallic cabin with one person working in it. The parameters W_1, W_2, L_1, L_2 and H are the rooftop width, floor width, rooftop length, floor length, and cabin height, respectively. The cabin has one door and several windows with different shapes, and it is illuminated by single or even double IEMPs with different power levels, incident directions and polarizations.

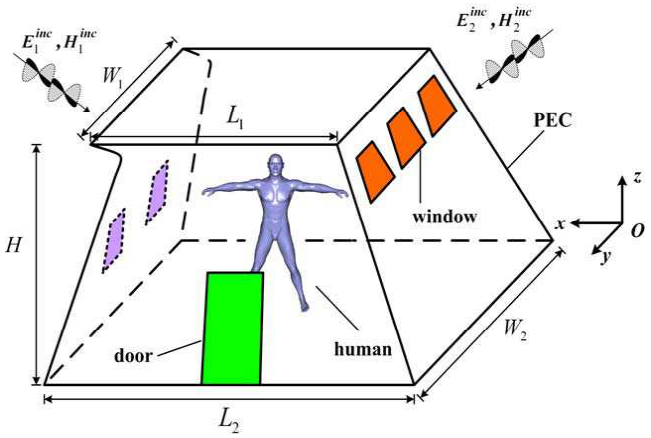

Figure 1. A cabin with one person in it.

In Fig. 1, the incident IEMP is assumed to be an ultra wideband pulse (UWBP), and its incident E-field can be described by a triple-exponential function as given by [25]

$$E_{inc} = \sum_{p=1}^{3} \frac{a^{(p)}}{b^{(p)}\sqrt{\pi/2}} \exp\left[-2\left(\left(t - t^{(p)}\right)/\tau^{(p)}\right)^2\right] \tag{1}$$

where one set of typical values of the coefficients $a^{(p)}$, $b^{(p)}$, $t^{(p)}$ and $\tau^{(p)}$ is summarized in Table 1. This triple-exponential UWBP is one typical waveform used in some high power EMP weapons.

Table 1. Pulse parameters of the triple-exponential UWBP.

Parameters (ns)	$a^{(p)}$	$b^{(p)}$	$t^{(p)}$	$\tau^{(p)}$
$p = 1$	1.55571	0.05207	0.07667	0.0521
$p = 2$	0.44016	0.05689	0.24527	0.0569
$p = 3$	5.07040	0.08847	0.11903	0.0885

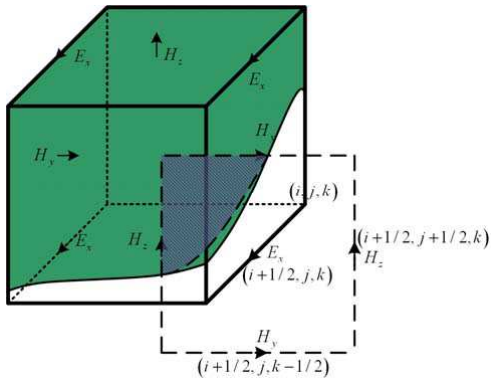

Figure 2. The adopted conformal mesh in the x-direction.

3. NUMERICAL METHOD

3.1. Dielectric Conformal Technique

As shown in Fig. 2, different from the PEC conformal technique [29], we treat the FDTD cells on the curved object surface according to magnetic grids instead of electric ones. The dashed lines in Fig. 2 show the perpendicular-x-direction face of one conformal mesh, whose central coordinates are denoted by $(i + 1/2, j, k)$. It is further used to modify permittivity and conductivity of the cutting face $(i + 1/2, j, k)$ which is related to the updated electric field component of E_x.

In Fig. 2, only one quarter of conformal face is in the Yee's cell. In practice, the whole conformal mesh face should be in four neighbouring cells. We further plot the conformal mesh face as shown in Fig. 3(a), where $S^{(1)}$ is the area of Medium 1 in it; $\{\varepsilon_1, \sigma_1\}$ and $\{\varepsilon_0, \sigma_0\}$ are the permittivities and the conductivities of Medium 1 and free space, respectively. Fig. 3(b) shows the face of modified mesh in Fig. 3(a), where S is its area. Therefore, both effective permittivity ε_x^{eff} and conductivity σ_x^{eff} at $(i + 1/2, j,k)$ are obtained by the weighted area,

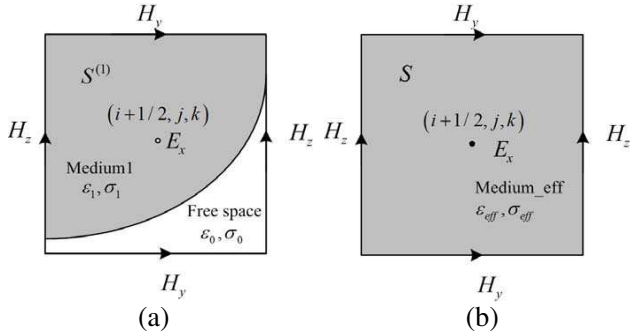

Figure 3. (a) Conformal mesh with Medium 1 and free space, and (b) modified mesh with effective permittivity and conductivity.

i.e.,

$$\varepsilon_x^{eff}(i+1/2,j,k)=\left[S^{(1)}(i+1/2,j,k)\times\varepsilon_1+\left(S-S^{(1)}(i+1/2,j,k)\right)\times\varepsilon_0\right]/S \quad (2)$$

$$\sigma_x^{eff}(i+1/2,j,k)=\left[S^{(1)}(i+1/2,j,k)\times\sigma_1+\left(S-S^{(1)}(i+1/2,j,k)\right)\times\sigma_0\right]/S \quad (3)$$

Further, the time stepping irritation of $E_x\,(i+1/2,\ j,\ k)$ can be derived according to the conformal meshes as given by:

$$\begin{aligned} &E_x^{n+1}(i+1/2,j,k) = CA_x \cdot E_x^n(i+1/2,j,k) \\ &+CB_x\cdot\left\{\left[H_z^{n+1/2}(i+1/2,j+1/2,k)-H_z^{n+1/2}(i+1/2,j-1/2,k)\right]/\Delta y\right. \\ &\left.-\left[H_y^{n+1/2}(i+1/2,j,k+1/2)-H_y^{n+1/2}(i+1/2,j,k-1/2)\right]/\Delta z\right\} \end{aligned} \quad (4)$$

where

$$CA_x=\left[1-\frac{\sigma_x^{eff}\,(i+1/2,j,k)\,\Delta t}{2\varepsilon_x^{eff}\,(i+1/2,j,k)}\right]\Bigg/\left[1+\frac{\sigma_x^{eff}\,(i+1/2,j,k)\,\Delta t}{2\varepsilon_x^{eff}\,(i+1/2,j,k)}\right] \quad (5)$$

$$CB_x=\left[\frac{\Delta t}{\varepsilon_x^{eff}\,(i+1/2,j,k)}\right]\Bigg/\left[1+\frac{\sigma_x^{eff}\,(i+1/2,j,k)\,\Delta t}{2\varepsilon_x^{eff}\,(i+1/2,j,k)}\right] \quad (6)$$

Following the similar procedure used above, both effective permittivities $\{\varepsilon_y^{eff},\ \varepsilon_z^{eff}\}$ and conductivities $\{\sigma_y^{eff},\ \sigma_z^{eff}\}$ can also be calculated. Therefore, the update equations of $E_y\,(i,\ j+1/2,\ k)$ and $E_z\,(i,\ j,\ k+1/2)$ can be derived. As the media involved are nonmagnetic, it is not necessary to modify the H-field iteration equations in our conformal FDTD method. For the cells which are totally in Medium 1, the corresponding E-field iteration equations are the same as those in the traditional FDTD method.

3.2. Computation of SAR

Having obtained the E-field values in the FDTD domain, we can compute the point SAR as follows:

$$\begin{aligned}\mathrm{SAR}\,(i+1/2,j+1/2,k+1/2) &= \frac{1}{2\rho\,(i+1/2,j+1/2,k+1/2)}\\ &\Big[\sigma_x\,(i+1/2,j+1/2,k+1/2)\cdot|E_x\,(i+1/2,j+1/2,k+1/2)|^2\\ &+\sigma_y\,(i+1/2,j+1/2,k+1/2)\cdot|E_y\,(i+1/2,j+1/2,k+1/2)|^2\\ &+\sigma_z\,(i+1/2,j+1/2,k+1/2)\cdot|E_z\,(i+1/2,j+1/2,k+1/2)|^2\Big] \quad (7)\end{aligned}$$

where ρ is the medium density [26]. We use the coordinates $(i+1/2,\ j+1/2,\ k+1/2)$ to represent the real centre of the cell. The conductivities of conformal meshes in the x-, y- and z-directions are computed above, together with the E-field values obtained by the FDTD iteration. These computed E-field results are just located on the centre of the FDTD cells edges, however, the SAR computation needs both E-field and conductivity results of the whole cell. Thus, we need to introduce interpolation schemes to get the corresponding E-field values and conductivities on the centre of the FDTD cells.

It is evident that, when the cells are totally in Medium 1, σ_x, σ_y and σ_z should be the ones of Medium 1 in the x-, y- and z-directions, respectively. Therefore, we compute E_x, E_y and E_z by

$$\begin{aligned}E_x\,(i+1/2,j+1/2,k+1/2) &= \frac{1}{4}\,[E_x(i+1/2,j,k)+E_x(i+1/2,j+1,k)\\ &+E_x(i+1/2,j,k+1)+E_x(i+1/2,j+1,k+1)] \quad (8)\\ E_y\,(i+1/2,j+1/2,k+1/2) &= \frac{1}{4}\,[E_y(i,j+1/2,k)+E_y(i+1,j+1/2,k)\\ &+E_y(i,j+1/2,k+1)+E_y(i+1,j+1/2,k+1)] \quad (9)\\ E_z\,(i+1/2,j+1/2,k+1/2) &= \frac{1}{4}\,[E_z(i,j,k+1/2)+E_z(i+1,j,k+1/2)\\ &+E_z(i,j+1,k+1/2)+E_z(i+1,j+1,k+1/2)]\,. \quad (10)\end{aligned}$$

When the cells are in the conformal ones, we compute σ_x, σ_y, and σ_z by using

$$\begin{aligned}\sigma_x\,(i+1/2,j+1/2,k+1/2) &= \frac{1}{N_x}\Big[\sigma_x^{eff}\,(i+1/2,j,k)\cdot B(i+1/2,j,k)\\ &+\sigma_x^{eff}\,(i+1/2,j+1,k)\cdot B(i+1/2,j+1,k)+\sigma_x^{eff}\,(i+1/2,j,k+1)\\ &\cdot B(i+1/2,j,k+1)+\sigma_x^{eff}\,(i+1/2,j+1,k+1)\cdot B(i+1/2,j+1,k+1)\Big]\end{aligned} \quad (11)$$

$$\sigma_y\left(i+1/2,j+1/2,k+1/2\right)=\frac{1}{N_Y}\left[\sigma_y^{eff}\left(i,j+1/2,k\right)\cdot B(i,j+1/2,k)\right.$$
$$+\sigma_y^{eff}\left(i+1,j+1/2,k\right)\cdot B\left(i+1,j+1/2,k\right)+\sigma_y^{eff}\left(i,j+1/2,k+1\right)$$
$$\left.\cdot B(i,j+1/2,k+1)+\sigma_y^{eff}\left(i+1,j+1/2,k+1\right)\cdot B(i+1,j+1/2,k+1)\right] \tag{12}$$

$$\sigma_z\left(i+1/2,j+1/2,k+1/2\right)=\frac{1}{N_Z}\left[\sigma_z^{eff}\left(i,j,k+1/2\right)\cdot B(i,j,k+1/2)\right.$$
$$+\sigma_z^{eff}\left(i+1,j,k+1/2\right)\cdot B(i+1,j,k+1/2)+\sigma_z^{eff}\left(i,j+1,k+1/2\right)$$
$$\left.\cdot B(i,j+1,k+1/2)+\sigma_z^{eff}\left(i+1,j+1,k+1/2\right)\cdot B(i+1,j+1,k+1/2)\right] \tag{13}$$

and E_x, E_y and E_z in (7) are computed by

$$E_x\left(i+1/2,j+1/2,k+1/2\right)=\frac{1}{N_x}\left[E_x(i+1/2,j,k)\cdot B(i+1/2,j,k)\right.$$
$$+E_x(i+1/2,j+1,k)\cdot B(i+1/2,j+1,k)+E_x(i+1/2,j,k+1)$$
$$\left.\cdot B(i+1/2,j,k+1)+E_x(i+1/2,j+1,k+1)\cdot B(i+1/2,j+1,k+1)\right] \tag{14}$$

$$E_y\left(i+1/2,j+1/2,k+1/2\right)=\frac{1}{N_y}\left[E_y(i,j+1/2,k)\cdot B(i,j+1/2,k)\right.$$
$$+E_y(i+1,j+1/2,k)\cdot B(i+1,j+1/2,k)+E_y(i,j+1/2,k+1)$$
$$\left.\cdot B(i,j+1/2,k+1)+E_y(i+1,j+1/2,k+1)\cdot B(i+1,j+1/2,k+1)\right] \tag{15}$$

$$E_z\left(i+1/2,j+1/2,k+1/2\right)=\frac{1}{N_Z}\left[E_z(i,j,k+1/2)\cdot B(i,j,k+1/2)\right.$$
$$+E_z(i+1,j,k+1/2)\cdot B(i+1,j,k+1/2)+E_z(i,j+1,k+1/2)$$
$$\left.\cdot B(i,j+1,k+1/2)+E_z(i+1,j+1,k+1/2)\cdot B(i+1,j+1,k+1/2)\right] \tag{16}$$

where N_x, N_y and N_z are the numbers of edges totally or partly in Medium 1 in the x-, y- and z-directions, respectively. In particular, when the edge is totally or partly in Medium 1, $B = 1$, and otherwise, it is zero. In this way, we exclude the E-field values totally outside Medium 1, which are easy to introduce additional errors at the object interface in the SAR computation.

Having obtained the point SAR values of all cells in the model, the average SAR can be computed by averaging them over the cells involved. For practical application, we need to compute point SAR, 1 g SAR and 10 g SAR inside the human head or the whole body model,

respectively. The averaged SAR over a reference mass 1 g and 10 g are computed according to the method described in [28].

4. NUMERICAL RESULTS AND DISCUSSION

Based on the above dielectric conformal FDTD method, numerical algorithm is developed for SAR computation, with its accuracy verified at first. Fig. 4(a) shows the computed point SAR distribution at $x = 0$ plane of one dielectric sphere with mesh size $\Delta x = \Delta y = \Delta z = 2\,\text{mm}$ illuminated by a sinusoidal electromagnetic (EM) wave of frequency 600 MHz. Its diameter is set to be 20 cm, the centre of sphere is at the origin of coordinate system. The results obtained by commercial software CST are also plotted in Fig. 4(b) for comparison. The relative permittivity, conductivity and mass density of the dielectric sphere are chosen to be $\varepsilon_r = 45.2$, $\sigma = 0.88\,\text{S/m}$, and $\rho = 1000\,\text{kg/m}^3$, respectively, which are similar to the physical constants of human tissue liquid [27]. The incident EM plane wave propagates along the z-direction, with its polarization in the x-direction and power density of $10\,\text{W/m}^2$. The time step is $\Delta t = \Delta x/2c$, where c is the light speed in free space. Ten-layered PML [26] is implemented for our computation.

To check the accuracy of our conformal FDTD method with coarse meshes used, Figs. 5(a) and (b) further show the point SAR obtained by our conformal FDTD method, the traditional FDTD method and CST. Two FDTD meshes are chosen for computation, i.e., $\Delta x = \Delta y = \Delta z = 2$ and 5 mm. Our conformal FDTD method adopts the 5 mm cell size, and it agrees well with the traditional FDTD with the mesh of 2 mm. In particular, it can generate accurate results at the sphere boundary of 0 and 200 mm, where the traditional FDTD method cannot predict the point SAR accurately. In Fig. 5(a), due to the effect of computation accuracy, the traditional FDTD results do not coincide with conformal FDTD or CST results very well from 90 mm to 110 mm at the centre of sphere, where there is a peak of the point SAR results.

To further quantify the accuracy of our method, we compute the maximum and average relative SAR errors of the results shown in Fig. 5 and the relevant 2 mm mesh size conformal method results shown in Fig. 4(a), which are defined by:

$$M_{ax-RE} = \frac{\max\left(\left|\text{SAR}\left(i,j,k\right) - \text{SAR}_{\text{CST}}\left(i,j,k\right)\right|\right)}{\max\left(\text{SAR}_{\text{CST}}\left(i,j,k\right)\right) - \min\left(\text{SAR}_{\text{CST}}\left(i,j,k\right)\right)} \tag{17}$$

and

$$A_{ve-RE} = \frac{\sum\limits_{i,j,k}\left|\text{SAR}\left(i,j,k\right) - \text{SAR}_{\text{CST}}\left(i,j,k\right)\right|}{N\left(\max\left(\text{SAR}_{\text{CST}}\left(i,j,k\right)\right) - \min\left(\text{SAR}_{\text{CST}}\left(i,j,k\right)\right)\right)} \tag{18}$$

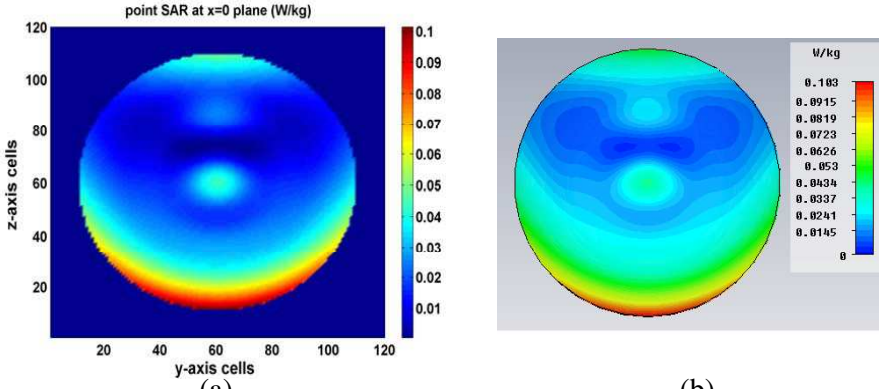

Figure 4. Distributions of point SAR on the x=0 plane obtained by (a) dielectric conformal FDTD method of 2 mm mesh size (b) CST MWS, respectively.

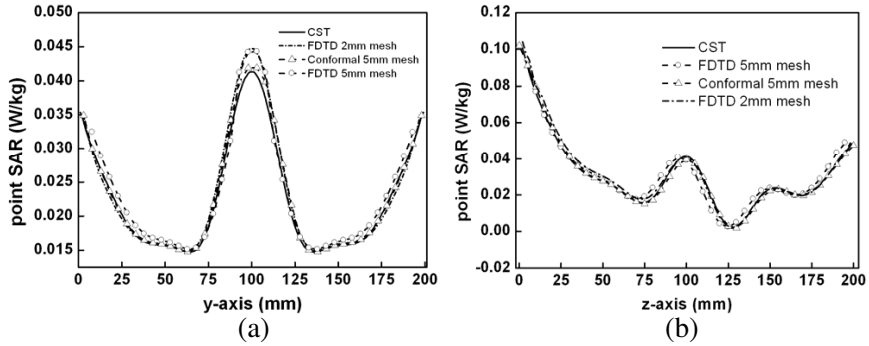

Figure 5. Comparison of the point SAR between the results obtained by conformal FDTD and CST MWS. (a) Along the y-axis ($x = z = 0$); and (b) along the z-axis ($x = y = 0$).

where N is the total cell number added in the numerator in (18). Both of them are summarized in Table 2 for comparison.

According to Table 2, we can see that our conformal FDTD method has less relative errors and better accuracy than that of traditional FDTD method even using 5 mm meshes. The wavelength of the 600 MHz sinusoidal EM wave in the dielectric sphere of $\varepsilon_r = 45.2$ is about $\lambda_d = 7.44$ cm, and therefore $\lambda_d/10 = 7.44$ mm. Actually, if the incident wavelength is longer than $\lambda_d/10$, the accuracy of our method is better than that of the traditional FDTD method.

Table 2. Comparison of M_{ax-RE} and A_{ve-RE} in the Computation of SAR.

Error Calculation	y-axis ($x = z = 0$)	z-axis ($x = y = 0$)
conformal (2 mm) M_{ax-RE} (%)	3.47	3.72
conformal (2 mm) A_{ve-RE} (%)	1.94	1.12
conformal (5 mm) M_{ax-RE} (%)	4.17	4.05
conformal (5 mm) A_{ve-RE} (%)	2.05	1.38
FDTD (2 mm) M_{ax-RE} (%)	10.6	9.4
FDTD (2 mm) A_{ve-RE} (%)	4.12	2.95
FDTD (5 mm) M_{ax-RE} (%)	13.2	11.6
FDTD (5 mm) A_{ve-RE} (%)	6.38	3.25

We now study the case of one human head model as shown in Figs. 6(a)–(d), which is illuminated by a sinusoidal EM wave of frequency 300 MHz and power density 10 W/m^2. The model is provided by the CST MWS, and it is also filled with the human tissue liquid, characterized by relative permittivity $\varepsilon_r = 45.3$, conductivity $\sigma = 0.87$ S/m [27], and mass density 1000 kg/m^3. The head centre is set at the origin of coordinate system. The incident plane wave propagates along the z-direction, and its polarization is in the x-direction polarization. In our conformal FDTD computation, the cell size is chosen to be $\Delta x = \Delta y = \Delta z = 2$ mm, the time step is $\Delta t = \Delta x/2c$, with 10-layered cell size PML used. In Figs. 6(a)–(d), it is observed that the maximum SAR appears at the back side of skull, as it is illuminated by the plane wave from the z-direction. Besides, the both maximum SAR and SAR distribution results obtained by the described method have good agreement with those of CST MWS. The difference of maximum SAR value between our table method and CST is smaller than 0.59%.

As the incident plane wave in Figs. 6(a)–(d) is replaced by an UWBP as described by (1), with its E-field amplitude increased from 200 to 1000 V/m gradually, Fig. 7 shows the maximum point SAR, 1 g SAR, 10 g SAR at the back side of skull of the human head model obtained by conformal FDTD method and that of CST MWS corresponding to $f = 300$ MHz. The human tissue is dispersive medium, and its constitutive parameters are all frequency-dependent and can be treated by differential-equation approach [30]. Here, we consider our concerned frequency $f = 300$ MHz. For the UWBP incidence, we transform its transient electric field values into frequency domain, and then calculate the SAR results according to the normalized E- field values at $f = 300$ MHz. As shown in Fig. 7, the

maximum values of point SAR, 1 g SAR, and 10 g SAR all increase monotonously with increasing the E-field amplitude of the incident IEMP.

Further, our attention is focused on the metallic cabin in Fig. 1 illuminated by an UWBP for different incident directions and polarizations, and one human body model is located at the middle of the cabin floor. The cabin model is developed according to one realistic warship platform. Its geometrical parameters, together with one door, several windows and body sizes, are all given in Figs. 8(a) and (b). Certainly, the cabin structure can be based on other designs for real

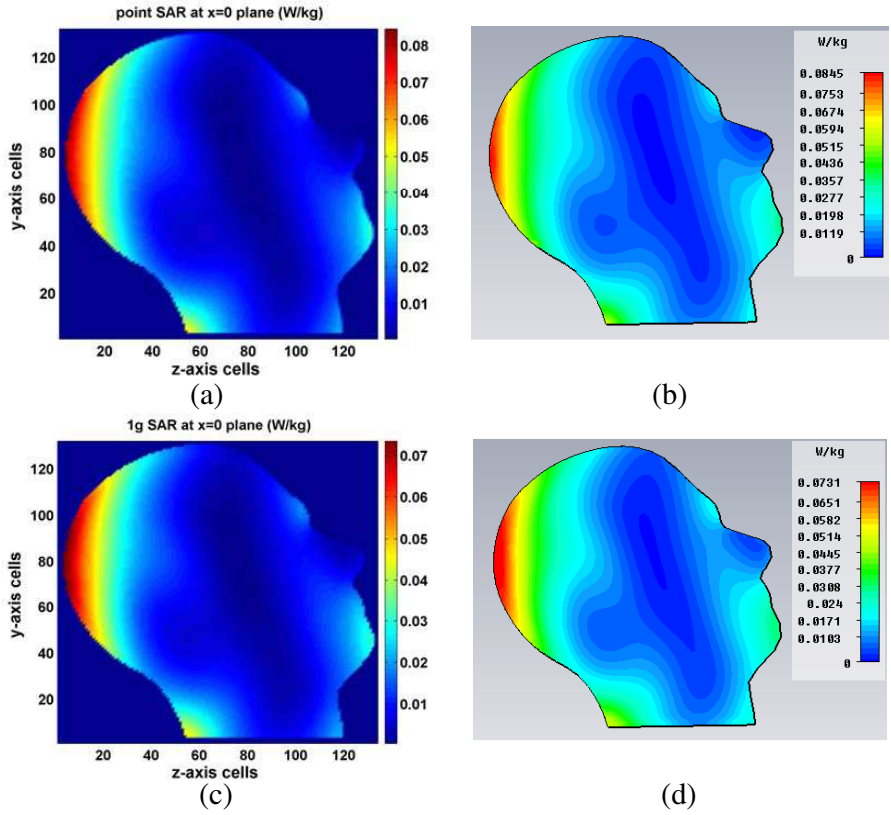

Figure 6. Distributions of the point SAR and 1 g SAR over the head model of 2 mm mesh size at $x = 0$ plane. Cases (a) and (b), point SAR computed by the conformal FDTD method and CST MWS, respectively. Cases (c) and (d), 1 g SAR computed by the same methods as in cases (a) and (b), respectively.

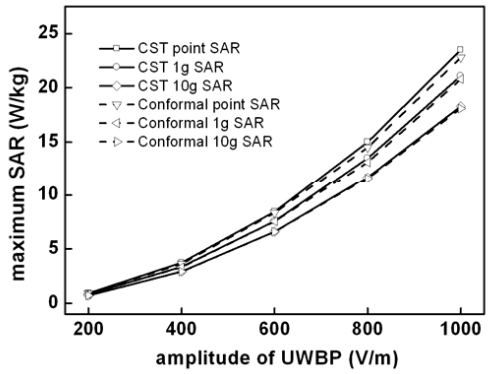

Figure 7. The maximum point SAR, 1 g SAR, and 10 g SAR ($x = 0$ plane) at the back side of skull of head model illuminated by an UWBP for different incident E-field amplitudes.

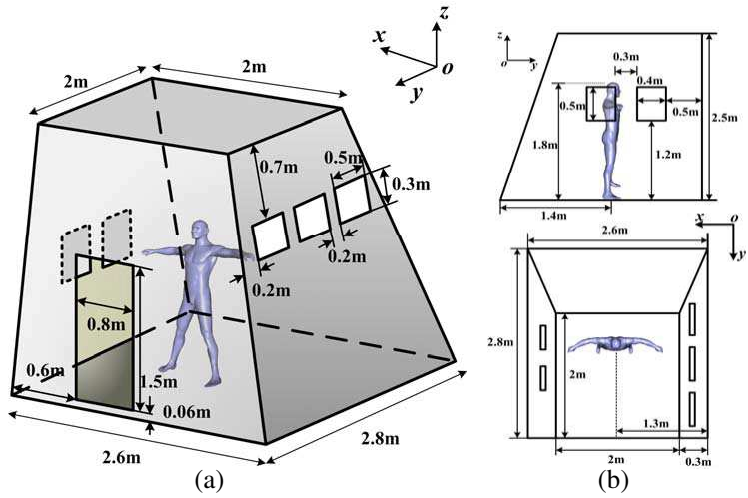

Figure 8. (a) Geometry of the cabin with one body model in it, and (b) views from both yz and xy planes.

applications, and the incident IEMP can take other forms. The model is also filled with the human tissue liquid, characterized by $\varepsilon_r = 45.3$, conductivity $\sigma = 0.87\,\mathrm{S/m}$ [27], and mass density $\rho = 1000\,\mathrm{kg/m^3}$. In our computation, the FDTD cells are set to be $\Delta x = \Delta y = \Delta z = 1\,\mathrm{cm}$, and we now consider two important cases as follows.

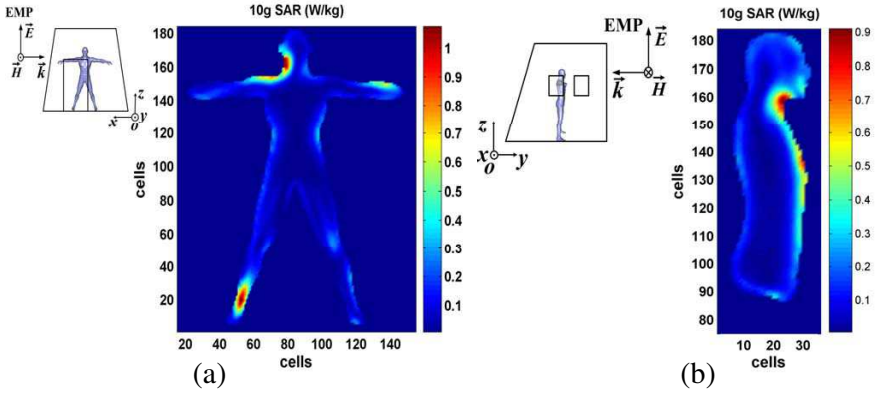

Figure 9. Distributions of 10 g SAR at $f = 300$ MHz over the body model at (a) $y = 0$ and (b) $x = 0$ planes, respectively.

4.1. Cabin Door Is Opened

We choose the incident UWBP amplitude to be 200 V/m, and it propagates (a) in $-x$- and (b) $-y$-direction, respectively. Figs. 9(a) and (b) show the computed 10 g SAR of the body model at $f = 300$ MHz. In Fig. 9(a), it is observed the right leg and neck parts absorb more incident EM energy than the other one of the body model. In Fig. 9(b), the front of body model absorbs more electromagnetic energy as the door is opened, and the maximum value of 10 g SAR is located at the throat region, which is about 0.9 W/kg.

In Fig. 9(b), as the E-field amplitude of the incident UWBP is increased from 200 to 400, 600, 800 and 1000 V/m, respectively, the maximum point SAR and 10 g SAR are observed at the throat region, both increases monotonously as shown in Fig. 10.

4.2. Cabin Door Is Closed

As the door is closed, we assume that the door and the front wall of the cabin is a continuous perfectly conducting surface. The incident UWBP, with its E-field amplitude 200 V/m assumed, propagates in $-x$- and $+y$-directions, respectively. The computed 10 g SAR of the body model at $f = 300$ MHz is plotted in Figs. 11(a) and (b), respectively.

In Figs. 11(a) and (b), as the cabin door is closed, inner self-resonance modes inside the metallic cabin can be easily excited during the UWBP illumination, and the EM energy stored distributes in one standing wave form. Under such circumstances, hot regions over the

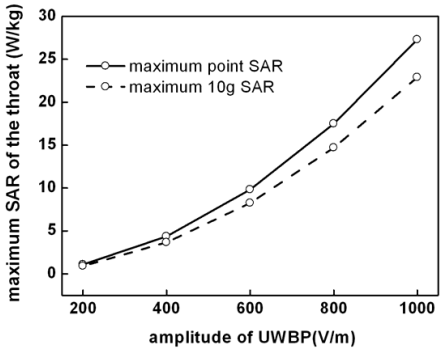

Figure 10. The maximum point SAR and 10 g SAR at $f = 300$ MHz at the throat of the body model as functions of the E-field amplitude of the incident UWBP.

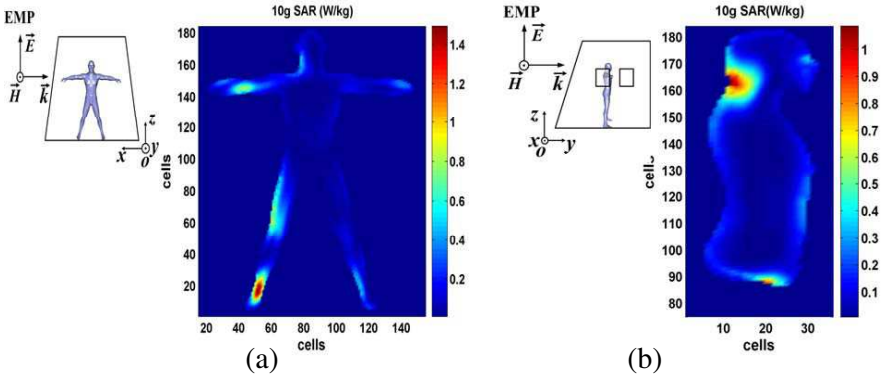

Figure 11. Distributions of 10 g SAR value at $f = 300$ MHz over the body model at (a) $y = 0$ and (b) $x = 0$ planes, respectively.

body model are directly related to the inner self-resonance modes, which result in the body model absorbing more EM energy than that the case of door is opened. The maximum SAR value in Fig. 11(a) appears over the right ankle of the body model, and it is similar to that in Fig. 9(a). The corresponding maximum SAR value here is about 1.48 W/kg, which is larger than that of 1.08 W/kg in Fig. 9(a). In Fig. 11(b), the nape and both eyes of the body model absorb more EM energy than that of the other body parts, and the maximum SAR value at the nape is about 1.1 W/kg.

As the incident UWBP propagates towards $+y-$direction, and its E-field amplitude is further increased from 200 to 1000 V/m, the

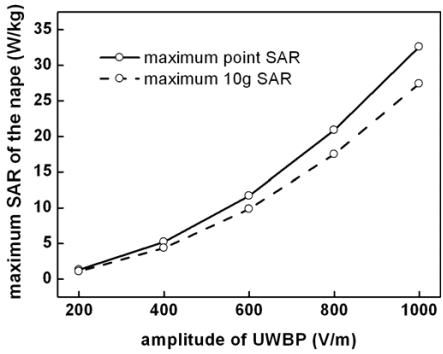

Figure 12. The maximum point SAR and 10 g SAR values at $f = 300$ MHz at the nape of the body model as a function of the E-field amplitude of the incident UWBP.

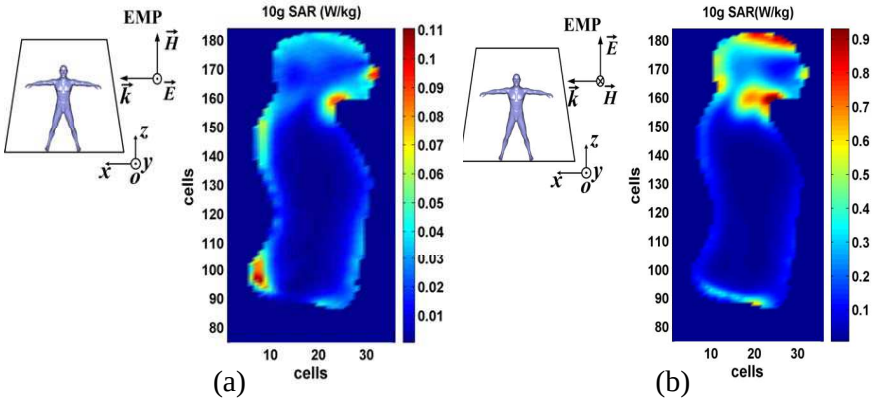

Figure 13. The 10 g SAR values at $f = 300$ MHz over the body model recorded at $y = 0$ plane. (a) The incident UWBP propagates towards $+x$-direction, with its polarization in $+y$-direction, and (b) the incident UWBP propagates towards $+x$-direction, with its polarization in $+z$-direction.

recorded maximum point SAR and 10 g SAR values at the nape are shown in Fig. 12.

4.3. Incident UWBP Polarizations

As the cabin door is closed, we suppose the incident UWBP propagates in the $+x$-direction, with its E-field amplitude 200 V/m chosen, but its polarization is in $+y$- and $+z$-directions, respectively. The 10 g SAR values over the body model recorded at $y = 0$ plane are plotted in Figs. 13(a) and (b), respectively.

It is observed that the 10 g SAR distributions are also sensitive to the variation of the incident UWBP polarization. In Fig. 13(a), the front and back side parts of the body model absorb more EM energy. For example, the maximum SAR values of the nose and hip parts are about 0.09 and 0.1 W/kg, respectively. In Fig. 13(b), the maximum SAR value appears at the throat part, which is about 0.92 W/kg.

5. CONCLUSION

In this paper, we have used one novel dielectric conformal finite-difference time-domain (FDTD) method for predicting specific absorption rate (SAR) distribution of the human body model in one metallic cabin of large geometry, which is illuminated by an intentional electromagnetic pulse (IEMP) with high power. Our improved conformal FDTD method introduce some effective dielectric parameters using the area average concept related to magnetic mesh to modify the E field update equations, and it is different from the traditional ones. Our developed conformal FDTD algorithm has been verified by calculating both point and average SAR distributions of dielectric sphere and human head models, respectively, where traditional FDTD method and commercial software CST MWS have also been used for accuracy comparison in the maximum and average relative errors of the computed SAR values. Numerical calculations are further carried out to capture the maximum SAR values over the human body model located in one large metallic cabin for different intentional UWBP incidences. It is believed that this study can provide some important information for electromagnetically protecting some persons working in high power exposure environment on certain large platform.

ACKNOWLEDGMENT

The authors appreciate the financial support of the NSF under Grant of 60831002 of China. Wen-Yan Yin also appreciates the financial support from the State Key Lab of Science and Technology of EMC, the Centre for Ship Development and Design of China.

REFERENCES

1. Giri, D. V. and F. M. Tesche, "Classification of intentional electromagnetic environments (IEME)," *IEEE Trans. on Electromagn. Compat.*, Vol. 46, No. 3, 322–328, Aug. 2004.

2. Wang, J., W.-Y. Yin, J.-P. Fang, and Q.-F. Liu, "Transient responses of coaxial cables in an electrically large cabin with slots and windows illuminated by an electromagnetic pulse," *Progress In Electromagnetics Research*, Vol. 106, 1–16, 2010.
3. Lei, J.-Z., C.-H. Liang, and Y. Zhang, "Study on shielding effectiveness of metallic cavities with apertures by combing parallel FDTD method with windowing technique," *Progress In Electromagnetics Research*, Vol. 74, 85–112, 2007.
4. Wang, Y. J., W. J. Koh, C. K. Lee, and K. Y. See, "Electromagnetic coupling analysis of transient signal through slots or apertures perforated in a shielding metallic enclosure using FDTD methodology," *Progress In Electromagnetics Research*, Vol. 36, 247–264, 2002.
5. Kusuma, A. H., A.-F. Sheta, I. Elshafiey, Z. Siddiqui, M. A. S. Alkanhal, S. Aldosari, S. A. Alshebeili, and S. F. Mahmoud, "A new low SAR antenna structure for wireless handset applications," *Progress In Electromagnetics Research*, Vol. 112, 23–40, 2011.
6. Attardo, E. A., T. Isernia, and G. Vecchi, "Field synthesis in inhomogeneous media: Joint control of polarization, uniformity and SAR in MRI B_1-field," *Progress In Electromagnetics Research*, Vol. 118, 355–377, 2011.
7. Khalatbari, S., D. Sardari, A. A. Mirzaee, and H. A. Sadafi, "Calculating SAR in two models of the human head exposed to mobile phones radiations at 900 and 1800 MHz," *PIERS Online*, Vol. 2, No. 1, 104–109, 2006.
8. Zheng, H.-X., X.-Q. Sheng, and E. K.-N. Yung, "Computation of scattering from anisotropically coated bodies using conformal FDTD," *Progress In Electromagnetics Research*, Vol. 35, 287–297, 2002.
9. Kouveliotis, N. K. and C. N. Capsalis, "Prediction of the SAR level induced in a dielectric sphere by a thin wire dipole antenna," *Progress In electromagnetic Research*, Vol. 80, 321–336, 2008.
10. Simba, A. Y., T. Hikage, S. Watanabe, and T. Nojima, "Specific absorption rates of anatomically realistic human models exposed to RF electromagnetic fields from mobile phones used in elevators," *IEEE Trans. on Microw. Theory and Tech.*, Vol. 57, No. 5, 1250–1259, May 2009.
11. Zhang, M. and A. Alden, "Calculation of whole-body SAR from a 100 MHz diploe antenna," *Progress In Electromagnetics Research*, Vol. 119, 133–153, 2011.

12. Ebrabimi-Ganjeh, M. A. and A. R. Attari, "Interaction of dual band helical and PIFA handset antennas with human head and hand," *Progress In Electromagnetics Research*, Vol. 77, 225–242, 2007.
13. Hirata, A., K. Shirai, and O. Fujiwara, "On averaging mass of SAR correlating with temperature elevation due to a dipole antenna," *Progress In Electromagnetics Research*, Vol. 84, 221–237, 2008.
14. Christopoulou, M., S. Koulouridis, and K. S. Nikita, "Parametric study of power absorption patterns induced in about and child head models by small helical antennas," *Progress In Electromagnetics Research*, Vol. 94, 49–67, 2009.
15. Mohsin, S. A., "Concentration of the specific absorption rate around deep brain stimulation electrodes during MRI," *Progress In Electromagnetics Research*, Vol. 121, 469–484, 2011.
16. Gemio, J., J. Parron, and J. Soler, "Human body effects on implantable antennas for ISM bands applications: Models comparison and propagation losses study," *Progress In Electromagnetics Research*, Vol. 110, 437–452, 2010.
17. Iero, D., T. Isernia, A. F. Morabito, I. Catapano, and L. Crocco, "Optimal constrained field focusing for hyperthermia cancer therapy: A feasibility assessment on realistic phantoms," *Progress In Electromagnetics Research*, Vol. 102, 125–141, 2010.
18. Vaccari, A., A. Cala' Lesina, L. Cristoforetti, and R. Pontalti, "Parallel implementation of a 3D subgridding FDTD algorithm for large simulations," *Progress In Electromagnetics Research*, Vol. 120, 263–292, 2011.
19. Neufeld, E., N. Chavannes, T. Samaras, and N. Kuster, "Novel conformal technique to reduce staircasing artifacts at material boundaries for FDTD modeling of the bioheat equation," *Phys. Med. Biol.*, Vol. 52, 4371–4381, 2007.
20. Yu, W. and R. Mittra, "A conformal finite difference time domain technique for modeling curved dielectric surfaces," *IEEE Microwave Wireless Comp. Lett.*, Vol. 11, No. 1, 25–27, Jan. 2001.
21. Yu, W., D. Arakaki, and R. Mittra, "On the solution of a class of large body problems with full or partial circular symmetry by using the finite-difference time-domain (FDTD) method," *IEEE Trans. on Antennas and Propag.*, Vol. 48, No. 12, 1810–1817, Dec. 2000.
22. Hu, X.-J. and D.-B. Ge, "Study on conformal FDTD for electromagnetic scattering by targets with thin coating," *Progress In Electromagnetics Research*, Vol. 79, 305–319, 2008.

23. Zheng, H.-X., X.-Q. Sheng, and E. K.-N. Yung, "Computation of scattering from anisotropically coated bodies using conformal FDTD," *Progress In Electromagnetics Research*, Vol. 35, 287–297, 2002.
24. Wang, J., W.-Y. Yin, P.-G. Liu, and Q.-H. Liu, "High-order interface treatment techniques for modeling curved dielectric objects," *IEEE Trans. on Antennas and Propag.*, Vol. 58, No. 9, 2946–2953, Sep. 2010.
25. Prather, W. D., C. E. Baum, R. J. Torres, F. Sabath, and D. Nitsch, "Survey of worldwide high-power wideband capabilities," *IEEE Trans. on Electromagn. Compat.*, Vol. 46, No. 3, 335–344, Aug. 2004.
26. IEEE C95.3, "IEEE recommended practice for measurements and computations of radio frequency," *IEEE Recommended Practice for Measurements and Computations of Radio Frequency*, IEEE, New York, 2002.
27. CENELEC, EN 50383, "Basic standard for the calculation and measurement of electromagnetic field strength and SAR related to human exposure from radio base stations and fixed terminal stations for wireless telecommunication systems (110 MHz–40 GHz)," 2002.
28. Koulouridis, S. and K. S. Nikita, "Study of the coupling between human head and cellular phone helical antennas," *IEEE Trans. on Electromagn. Compat.*, Vol. 46, No. 1, 62–70, Feb. 2004.
29. Jurgens, T. G., A. Taflove, K. R. Umashankar, and T. G. Moore, "Finite-difference time-domain modeling of curved surfaces," *IEEE Trans. on Antennas and Propagation*, Vol. 40, No. 4, 357–366, Apr. 1992.
30. Gandhi, O. P., B.-Q. Gao, and J.-Y. Chen, "A frequency-dependent finite-difference time-domain formulation for induced current calculations in human beings," *Bio. Electro. Magnetics*, Vol. 13, No. 6, 543–555, Mar. 1992.